Journal of Advanced Ceramics
2022, **11**(4): 570–581
https://doi.org/10.1007/s40145-021-0557-z
ISSN 2226-4108
CN 10-1154/TQ

Research Article

Preparation and properties of T-ZnO_w enhanced BCP scaffolds with double-layer structure by digital light processing

Ming-Zhu PAN[a,b,†], Shuai-Bin HUA[a,b,†], Jia-Min WU[a,b,*], Xi YUAN[c], Ze-Lin DENG[a,b], Jun XIAO[c], Yu-Sheng SHI[a,b]

[a]*State Key Laboratory of Materials Processing and Die & Mould Technology*, *School of Materials Science and Engineering*, *Huazhong University of Science and Technology*, *Wuhan 430074*, *China*
[b]*Engineering Research Center of Ceramic Materials for Additive Manufacturing*, *Ministry of Education*, *Wuhan 430074*, *China*
[c]*Department of Orthopedic Surgery*, *Tongji Hospital*, *Tongji Medical College*, *Huazhong University of Science and Technology*, *Wuhan 430030*, *China*

Received: August 11, 2021; Revised: November 9, 2021; Accepted: November 24, 2021

Abstract: Bone scaffolds require both good bioactivity and mechanical properties to keep shape and promote bone repair. In this work, T-ZnO_w enhanced biphasic calcium phosphate (BCP) scaffolds with triply periodic minimal surface (TPMS)-based double-layer porous structure were fabricated by digital light processing (DLP) with high precision. Property of suspension was first discussed to obtain better printing quality. After sintering, T-ZnO_w reacts with β-tricalcium phosphate (β-TCP) to form $Ca_{19}Zn_2(PO_4)_{14}$, and inhibits the phase transition to α-TCP. With the content of T-ZnO_w increasing from 0 to 2 wt%, the flexural strength increases from 40.9 to 68.5 MPa because the four-needle whiskers can disperse stress, and have the effect of pulling out as well as fracture toughening. However, excessive whiskers will reduce the cure depth, and cause more printing defects, thus reducing the mechanical strength. Besides, T-ZnO_w accelerates the deposition of apatite, and the sample with 2 wt% T-ZnO_w shows the fastest mineralization rate. The good biocompatibility has been proved by cell proliferation test. Results confirmed that doping T-ZnO_w can improve the mechanical strength of BCP scaffolds, and keep good biological property, which provides a new strategy for better bone repair.

Keywords: biphasic calcium phosphate (BCP); T-ZnO_w; digital light processing (DLP); double-layer structure; cure property; mechanical strength

1 Introduction

Bone defects have been a serious problem, which threaten more than 2 million people's health every year [1]. When the bone defect is larger than a certain size, self-repair becomes quite difficult [2]. At this time, bone tissue engineering (BTE), which combines well-designed scaffolds with signaling factors to provide cell adhesion, proliferation, and function [3,4], could perfectly address this problem. To get an ideal scaffold, both well-designed bioactive materials and porous structure are required [5].

† Ming-Zhu Pan and Shuai-Bin Hua contributed equally to this work.

* Corresponding author.
E-mail: jiaminwu@hust.edu.cn

Ca/P ceramic is one of the most promising material for bone scaffold because of its similar element component to natural bone [6]. Hydroxyapatite ($Ca_{10}(PO_4)_6(OH)_2$, HA) and β-tricalcium phosphate ($Ca_3(PO_4)_2$, β-TCP) have been widely used in bone scaffold, and biphasic calcium phosphate (BCP), the mixture of them, has a suitable degradation rate and mechanical properties [7–10]. However, the bioactivity and strength of BCP ceramic still need to be enhanced. Some people tried to improve the bone repair ability and strength of ceramic by adding ions such as Fe [11,12], Ag [13,14], Zr [15], Zn, and so on. Zn is one of the essential trace elements in the human body. The total weight of Zn in human body is about 1.4–2.3 g, with about 50% deposit in bones [16,17]. Tetrapod-like zinc oxide whisker (T-ZnO_w) is the only one of whiskers that has a spatial structure: Four needles of it stretch to different directions, offering an isotropic performance and helping to improve mechanical properties [18–21]. At the same time, T-ZnO_w shows excellent antibacterial properties and good biocompatibility [22,23], which is beneficial to scaffolds used for implanting. Therefore, the addition of T-ZnO_w is hopeful to enhance the strength and bone repair ability of composite bioceramics.

Good scaffolds require not only suitable material but also porous structure to induce cells to grow in. Pores' size, distribution, shape, and connection condition all have great impact on the performance of scaffolds [24–26]. Triply periodic minimal surface (TPMS) is a commonly-used structure. The curvature of any point on the surface of TPMS structure is zero, so stress can be uniformly distributed to avoid the damage caused by stress concentration. By adjusting parameters, the pore size and repeating unit of TPMS can be adjusted to meet different requirements [27,28]. However, it is hard for traditional methods to fabricate this structure considering the complexity, and fortunately, additive manufacturing (AM) techniques, including selective laser sintering (SLS) [29,30], direct ink writing (DIW) [31], stereolithography (SL) [32], digital light processing (DLP) [33,34], and so on, provide a new way to solve this problem by printing layer by layer [35,36]. Compared with other AM methods, DLP is based on suspension and more suitable to fabricate complex ceramic scaffolds with high precision [37].

The rheological property and cure property of suspension have great influence on DLP printing, and need to be studied to get high precision. Li *et al*. [38] investigated the cure depth and excess cure width of the suspension with different kinds of ZrO_2 powders, and found that as the colorant content increases, the cure depth and excess cure width both decrease due to the ceramic absorbance. Zheng *et al*. [39] researched the size distribution of ternary Al_2O_3 particles and their effect on the rheology of ceramic suspension. An optimized proportion formula was derived to get the suspension for DLP with high solid loading and low viscosity. T-ZnO_w has different particle morphology and optical properties from BCP, but researches on BCP suspension containing T-ZnO_w are still inadequate. It is necessary to investigate the viscosity and cure depth of suspension containing T-ZnO_w to achieve the best printing quality.

In this work, T-ZnO_w enhanced BCP scaffolds with TPMS-based double-layer porous structure were fabricated by DLP technology. The rheological and cure property of suspension was first discussed. Then phase composition, microstructure, shrinkage, volume density, and mechanical strength were tested to identify the influence of T-ZnO_w. Finally, apatite-forming ability and cell proliferation were investigated to verify the biological property.

2 Material and method

2. 1 Raw material

The ceramic powders were $Ca_{10}(PO_4)_6(OH)_2$ (HA, Kunshan Chinese Technology New Material Co., Ltd., China, index ≈ 1.665), $Ca_3(PO_4)_2$ (β-TCP, Kunshan Chinese Technology New Material Co., Ltd., China, index ≈ 1.626), and T-ZnO_w (Chengdu Crystrealm Co., Ltd., China, index ≈ 2.008). As shown in Figs. 1(a)–1(c), the powder of HA has the minimum size which is at nanoscale, while the size of β-TCP is much larger. The size of T-ZnO_w varied greatly with the length of needles ranging from 5 to 50 μm. The particle size distribution of BCP and T-ZnO_w is shown in Fig. 1(d). 1,6-hexanediol diacrylate (HDDA, Chengdu Fourth City New Material Co., Ltd., China) and tripropylene glycol diacrylate (TPGDA, Chengdu Fourth City New Material Co., Ltd., China) were used as the UV resin monomers. To get well-performed ceramic slurry, Solsperse 41000 (Lubrizol, Spain) was used as the dispersant. Diphenyl(2,4,6-trimethylbenzoyl) phosphine oxide (TPO, BASF, Germany) was chosen as the photoinitiator, and 4-methoxyphenol (MEHQ, Sinopharm Chemical Reagent Co., Ltd., China) was chosen as the photoinhibitor. Defoamer Foamex N (TEGO, Germany)

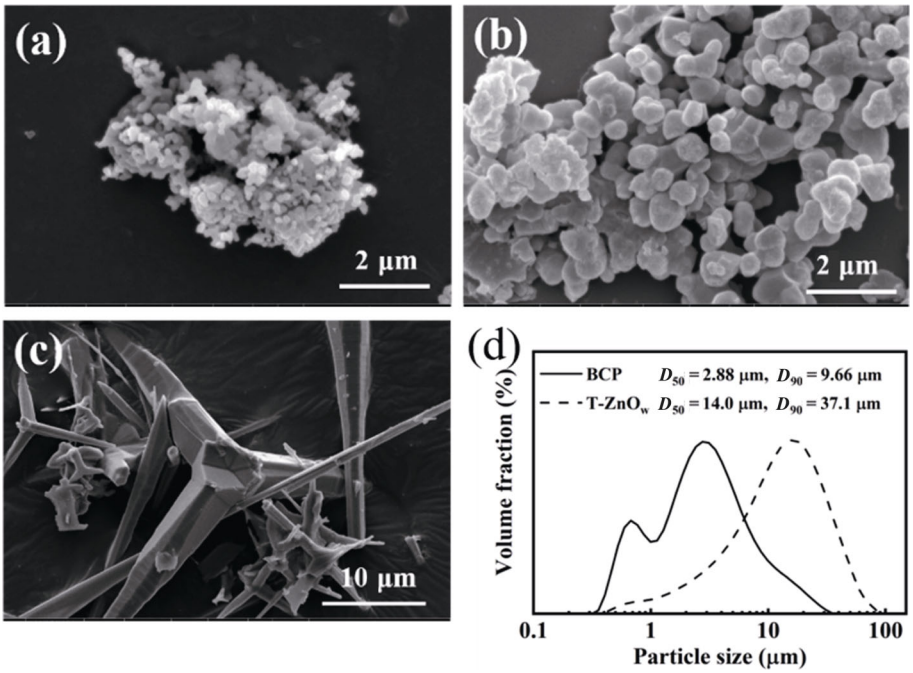

Fig. 1 Scanning electron microscopy (SEM) images of raw powders: (a) HA, (b) β-TCP, (c) T-ZnO$_w$; (d) particle size distribution of BCP and T-ZnO$_w$ powders.

was used to reduce the bubbles in suspension during printing. Simulated body fluid (SBF, Phygene Life Sciences Company Fujian, China) was used to test the scaffold's ability to interact with the body fluid after implantation.

2. 2 Fabrication of bone scaffolds

First, HDDA and TPGDA were mixed at the mass ratio of 7 ∶ 3. The mixture, together with Solsperse 41000 (4 wt% of ceramic powders) and Foamex N (0.1 wt% of ceramic powders), became the solvent after mixing evenly. Then, BCP (HA ∶ β-TCP = 6 ∶ 4) powders doped by different amount of T-ZnO$_w$ (0, 1, 2, and 3 wt% of ceramic powders, donated as Z0, Z1, Z2, Z3, respectively) were added into solvent, followed by stirring with a speed of 2800 r/min for 3 min in the vacuum planetary stirring defoaming machine (SIE-MIX80, Guangzhou Sienox Technology Co., Ltd., China). Solid loadings of all suspension were controlled at 40 vol%. Finally, TPO (2 wt% of total UV resin monomers) and MEHQ (0.2 wt% of total UV resin monomers) were added to prepare the final ceramic suspension for DLP. The TPMS-based double-layer scaffold model (diameter: 12.5 mm, height: 12.5 mm) with a 50% average porosity is shown in Fig. 2. The outer layer of the scaffold has a higher porosity (66%), which is beneficial for cells to grow in, while the inner layer is more compact (porosity 33%) to provide good mechanical properties. After being sliced by software with layer thickness set as 50 μm, models were printed by DLP printer (Autocera-M, Beijing Ten Dimensions Technology Co., Ltd., China) with a UV source of λ = 405 nm. Then the green bodies were cleaned in an ultrasonic bath to remove the uncured suspension. In the end, green bodies were debinded and sintered at 1200 ℃ as shown in Fig. 3.

2. 3 Characterization

The rheological property of suspensions with different T-ZnO$_w$ contents was examined by Discovery DHR-2 rheometer (TA Instrument, New Castle, USA), with the shear rate ascending from 0.1 to 50 s^{-1}. The cure property was measured by single-layer printing [40]. Cure depth (C_d) was tested by micrometer, and for each test five

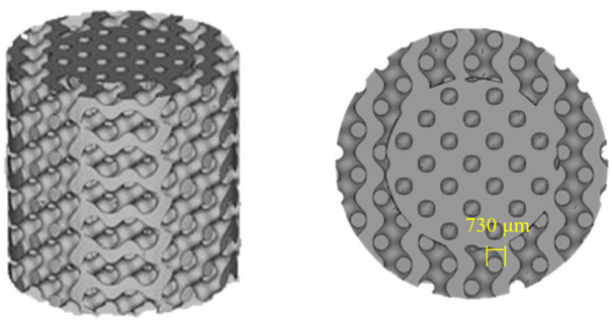

Fig. 2 Model of bone scaffolds.

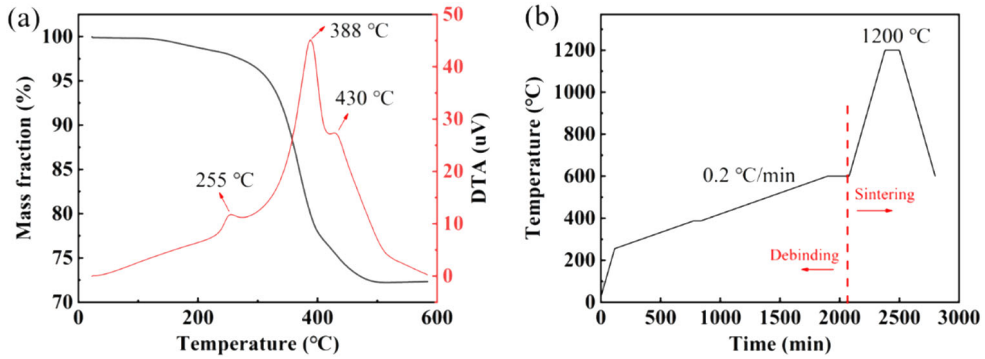

Fig. 3 (a) Thermogravimetric–differential thermal analysis (TG–DTA) of ceramic green body; (b) debinding and sintering curve.

independent thickness measurements were performed for averaging. Packing thickness was controlled at 800 μm.

To identify the influence of T-ZnO_w to sinterability, the volume density and shrinkage of samples were tested using solid discs. Volume density was obtained by the Archimedes method. Shrinkage of porous scaffold was calculated according to Eq. (1):

$$s = \frac{l_o - l_s}{l_o} \times 100\% \quad (1)$$

where l_o is the size before sintering, and l_s is the size after sintering. Three samples were tested for each composition. Scanning electron microscopy (SEM, Quanta650, FEI Company, USA) was used to observe the morphology of each sample, and X-ray diffraction (XRD, x'pert3 powder, PA Nalytical B.V., the Netherlands) was used to analyze the phase composition. Flexural strength was tested with a strip (5 mm × 4 mm × 40 mm) by three-point bending method, and compressive strength was tested with the porous double-layer scaffold shown in Fig. 2. The mechanical properties were all conducted on universal material testing machine (Zwick Z020, ZwickRoell, Germany).

2. 4 Biological test

Apatite-forming test was conducted to access the *in vitro* bioactivity of the samples. The samples were immersed in the SBF (the ratio of SBF volume to sample weight is 200 mL:1 g) and vibrated at 37 ℃. After 1, 7, and 14 d, samples from each group were taken out. The microstructure of the surface was observed by SEM, and the functional group was tested by Fourier transform infrared spectroscopy (FTIR, Nicolet iS50R, Thermo Scientific, USA). The SBF solution was filtered, and then the concentration of Ca^{2+} ion was tested by inductively coupled plasma optical emission spectrometer (ICP-OES, Prodigy Plus, Leeman Labs, USA) [41].

Considering high Zn^{2+} concentration may be toxic for cells, and the critical concentration remains controversial [42,43], cytotoxicity was analyzed by the proliferation of cultured cells in extraction fluid of bioceramics [44,45]. Samples were washed with ethanol and sterilized at 121 ℃ for 20 min. MC-3T3 cells were cultured in α-MEM (Gibico, USA) supplemented with 10% fetal bovine serum (FBS, Gibico, USA), 1% antimicrobial of streptomycin and penicillin in a humidified atmosphere at 37 ℃ with 5% CO_2. Cells at the third passage were used for the *in vitro* test. Cell counting kit (CCK-8, Boster, China) was used according to the manufacturer's protocol. To get the extraction fluid, every 200 mg bioceramic was immersed in 1 mL fluid and incubated at 37 ℃ for 24 h with a shaking speed of 120 r/min. Considering that the continuous flow of human blood would dilute the ion concentration, we prepared the extraction fluid diluted 4, 8, and 16 times at the same time. The cells were seeded at a density of 10^4 cells per well, and 100 μL extraction fluid was added to each well. After 1 and 3 d of cell culturing, 10 μL of CCK-8 reagent was added into the culturing medium 90 min before analysis at 37 ℃. The optical density (OD) values were read at 450 nm on an absorbance microplate reader (Bio-tek, USA).

3 Results and discussion

3. 1 Study on rheological and cure property of bioceramic suspension

The effect of T-ZnO_w content on rheological property is shown in Fig. 4. Figure 4(a) shows the viscosities of suspension. It can be seen that all suspensions show evident shear-thinning behavior which is beneficial for

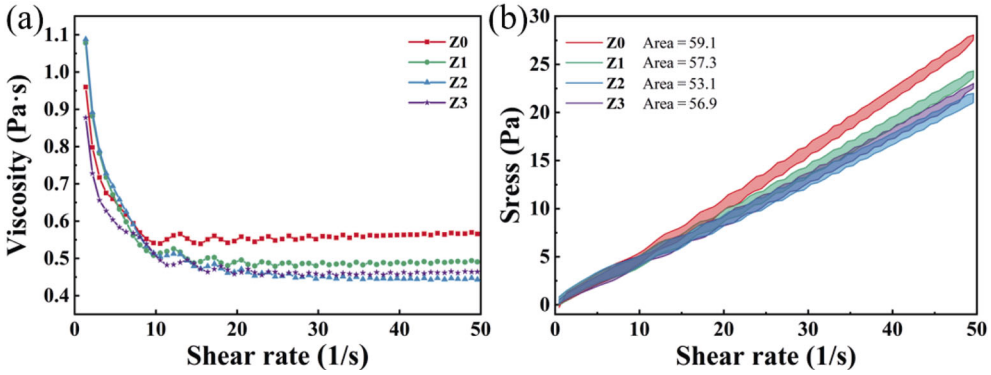

Fig. 4 Effect of T-ZnO_w content on (a) viscosity and (b) thixotropic loop of suspensions.

suspensions to spread out [46]. With the increase of T-ZnO_w content, the suspension viscosity decreases first and then increases. Z2 shows the lowest viscosity at about 0.45 Pa·s. Figure 4(b) exhibits the thixotropic loops. Area of the stress–shear rate loop, which can be calculated in Origin, reflects the thixotropy of suspension. Similar to the viscosity, the area of thixotropic loop also decreases first and then increases. Z2 has the smallest loop area, which means it is the easiest to recover after shearing, and help to reduce the formation of inner defect. With the increase of T-ZnO_w content, T-ZnO_w can impede the aggregation of HA and β-TCP particles considering the unique tetrapod-like structure of the whiskers shown in Fig. 1(c), lowering the viscosity and the area of thixotropic loop. However, when the content of T-ZnO_w keeps increasing, aggregation happens between whiskers [22], which reduce the dispersion effect, and increase the viscosity as well as the area of thixotropic loop.

As shown in Fig. 5, when lnE_i is 1.5, the cure depths are all larger than the printing layer thickness (50 μm). Though it can meet the energy required for monolayer curing, such cure is not thick enough to obtain a tight combination between layers, which makes it easy for samples to crack or even fall off during the printing process [33,47]. In the end, E_i = 12 mJ/cm^2 (lnE_i equals to 2.485) is chosen as the proper exposure energy, where the cure depth of suspension is about 90–110 μm, and Z3 has the smallest cure depth.

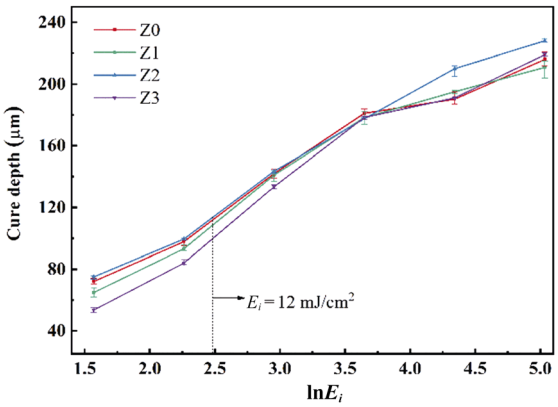

Fig. 5 Effect of T-ZnO_w content on cure depth of ceramic suspensions.

3. 2 Performance of T-ZnO_w doped BCP scaffolds

As shown in Fig. 6, double-layer porous scaffolds with high precision have been fabricated using the optimized printing parameters. From Figs. 6(a), 6(c), 6(e), and 6(g), it can be found that scaffolds are comprised of two parts, with high porosity outside and low porosity inside. Observing the enlarged figures (Figs. 6(b), 6(d), 6(f), and 6(h)), we can find that the surfaces of scaffolds are smooth on the whole except a few small pores on the surface caused by bubbles during the printing process. Z3 shows the worst accuracy compared with other samples considering that some of the pores outside are partly blocked. With the same exposure energy (dotted line in Fig. 5), Z3 has the lowest cure depth. In this way, more light is scattered and absorbed by surrounding suspension, resulting in excessive cure and decreased accuracy. Z0, Z1, and Z2 exhibit complete and interconnected pores with a pore size of about 500 μm, which is beneficial for the growth of bone tissue and blood vessel [48,49].

Figure 7 shows the phase composition of samples with different T-ZnO_w contents sintering at 1200 ℃. As for Z0, only TCP and HA (JCPDS 09-0432) can be examined, and TCP exists in both α-TCP (JCPDS 09-0348) and β-TCP (JCPDS 09-0169) since the phase transition can take place on β-TCP at high temperature [50]. With the increase of T-ZnO_w, HA shows no obvious differences, and remains to be the main phase, but obvious changes happen on TCP: Both β-TCP and α-TCP are weakened, and β-TCP almost disappears. $Ca_{19}Zn_2(PO_4)_{14}$ appears at the same time. These phenomena suggest that reaction

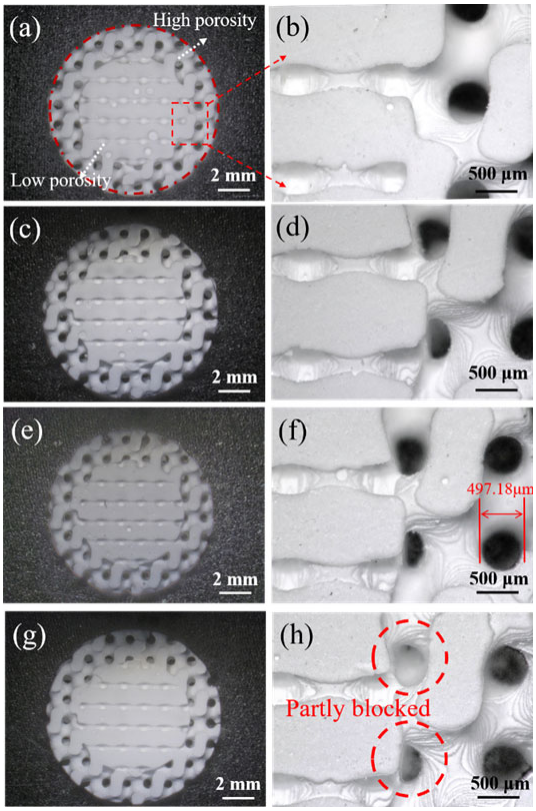

Fig. 6 Macroscopic images of scaffold's top-view: (a, b) Z0, (c, d) Z1, (e, f) Z2, and (g, h) Z3.

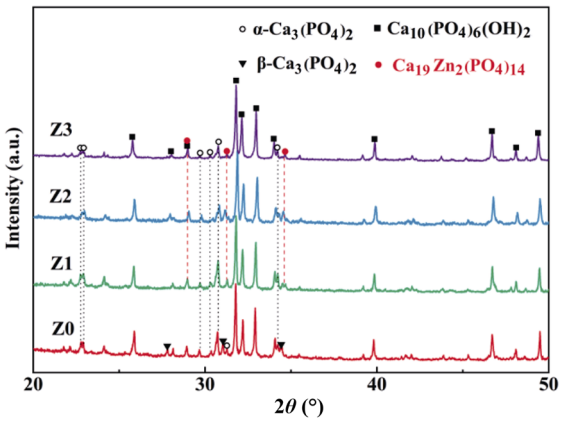

Fig. 7 XRD patterns of samples with different contents of T-ZnO_w.

took place between T-ZnO_w and β-TCP, causing the formation of new phase and inhibiting the phase transition [51].

Figure 8 shows the microscopic morphology of the sample surface and cross-section. It can be seen that there are still many pores in ceramics, and the pores left by T-ZnO_w can be observed clearly. The cross-section of Z2 is rougher than others. In addition, a large number of needle-like structures with a length of

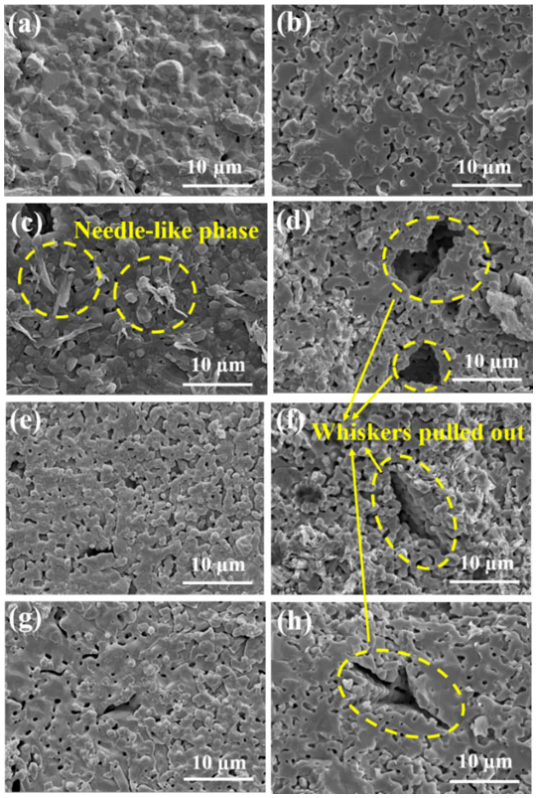

Fig. 8 SEM images of (a, b) Z0, (c, d) Z1, (e, f) Z2, and (g, h) Z3; (a, c, e, g) is the surface, and (b, d, f, h) is the cross-section.

about 10 μm can be seen on the surface and cross-section of Z1 (Figs. 8(c) and 8(d)) and the cross-section of Z2 (Fig. 8(f)), indicating that new phase may form here.

The shrinkage, volume density, and mechanical strength of samples sintered at 1200 ℃ are shown in Fig. 9. Figure 9(a) shows the shrinkage rate both in transverse and longitudinal directions, from which we can find that longitudinal shrinkage is always larger than transverse shrinkage owing to the poor interlayer connection during printing. With the increase of T-ZnO_w content, shrinkage and open density show no obvious difference. Figure 9(c) shows the flexural strength of the samples. With the content of T-ZnO_w increases from 0 to 2 wt%, the flexural strength increases from 40.9 to 68.5 MPa. When the content of T-ZnO_w keeps increasing to 3 wt%, the flexural strength decreases sharply to 49.4 MPa. This is because that four needles of T-ZnO_w can disperse the stress to four directions effectively. Fracture or pulling out of whiskers can also absorb energy and inhibit the propagation of crack, and thus the chance of damage can be reduced. Then as Fig. 10 shows, when the content of T-ZnO_w is 3 wt%, we can find that all fractures of Z3 show obvious step-like fracture, and

the defect between layers is more obvious than that of Z2. It can infer that the low cure depth of Z3 cause delamination, and in turn decrease the flexural strength. However, despite the weak combination of printing, flexural strength of Z3 is still larger than that of Z0, which proves that the addition of T-ZnO_w does help improve the flexural strength. The compressive strengths of Z0, Z1, Z2, and Z3 show no obvious difference (Fig. 9(d)), and that of Z2 (18.31 MPa) is a little higher than others, which is consistent with the flexural strength.

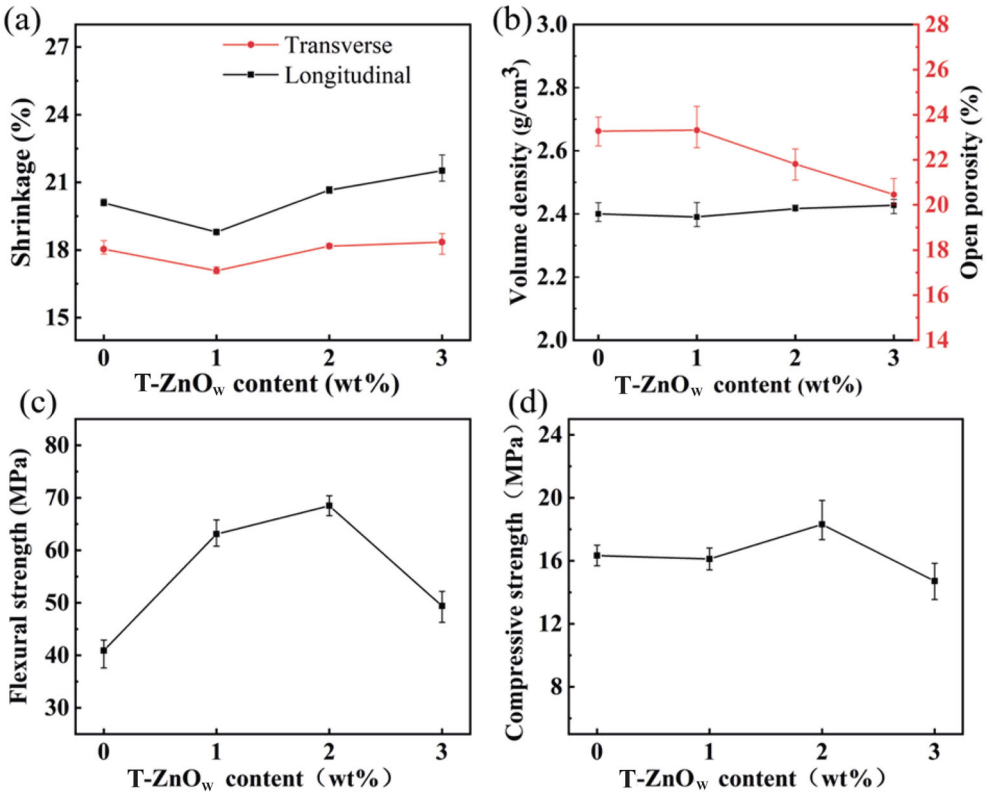

Fig. 9 Effect of T-ZnO_w content on the properties of samples sintered at 1200 ℃: (a) shrinkage, (b) volume density and open porosity, (c) flexural strength, and (d) compressive strength.

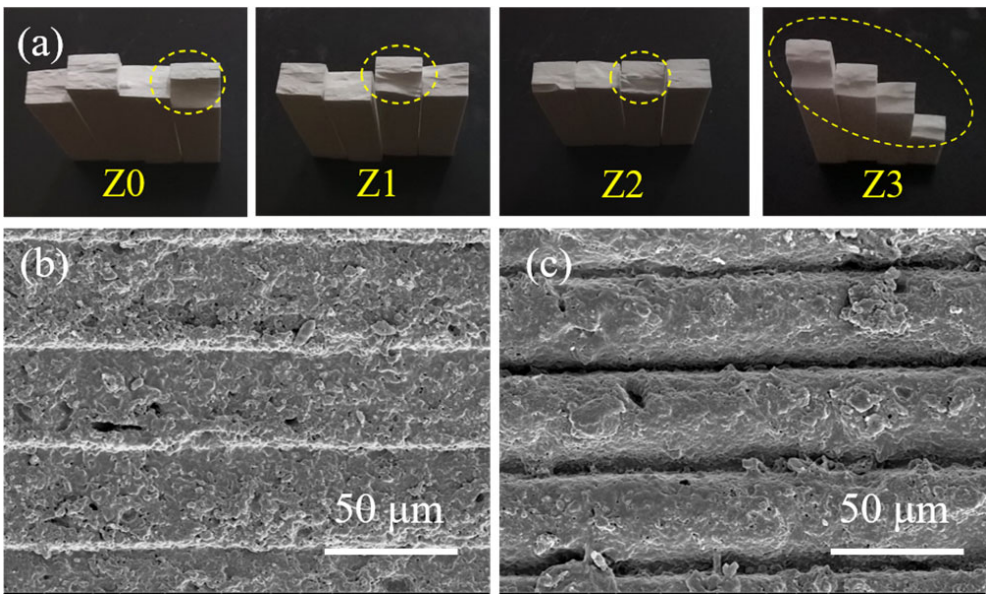

Fig. 10 (a) Cross-section of flexural samples; SEM images of interlayer bonding condition of (b) Z2 and (c) Z3.

3. 3 *In vitro* bioactivity

SEM images of the samples after soaking for 1, 7, and 14 d are shown in Fig. 11. It can be seen that after soaking for 1 d, Z2 has the fastest mineralization rate. Surfaces of Z0 and Z2 have been covered by villous substances obviously and segmented into serious of "shell". By contrast, Z1 and Z3 have not been covered completely, but the surface of them has become rougher compared with that before soaking, and some wormlike particles appeared. By testing the ion concentration in SBF, we can find that the Ca^{2+} concentration in Z2 is lower than others (Fig. 12(a)), which means more Ca^{2+} in SBF has deposited on the sample surface in the early stage, and formed the apatite mineralized layer. After soaking for 7 d, all the samples have been coated by villous substances intensively, forming a new spherical sediment layer with a diameter of about 4 μm, which is much larger than the original grain. The cracks in the sediment layer are caused by shrinkage during drying, proving that the sediment layer has a certain thickness.

After magnifying the surface (Fig. 12(b)), it can be observed that the villous material is a layer of dense wormlike particles with a length of 200–300 nm. Energy spectrum scanning shows that a large number of C atoms can be found in these particles, indicating that HCO_3^- ions in SBF solution may have been deposited on the surface. FTIR analysis exhibits the atom groups on the surface after soaking in SBF for 14 d (Fig. 12(c)). It shows strong absorption peaks of PO_4^{3-} near 563 and 1000 cm^{-1}, and absorption peaks of CO_3^{2-} functional group near 1430 cm^{-1} [52], which shows the existence of carbonated hydroxyapatite (CHA). CHA is similar to the inorganic components of natural bone in composition, and has large specific surface area. It can adsorb collagen, polysaccharide, and other substances, which is conducive to the adhesion and growth of osteoblast stem cells [53]. Therefore, the fast deposition rate of Z2 and well deposition of CHA on Z1 and Z3 proved that BCP ceramics containing T-ZnO_w exhibit good *in vitro* bioactivity.

To test the cytotoxicity of the samples, cell proliferation test was conducted. The results are shown in Fig. 13. We can find that the OD values of 3 d are all obviously larger than those of 1 d, which means cells can proliferate well at different dilution times. Besides, there is no obviously difference between samples with

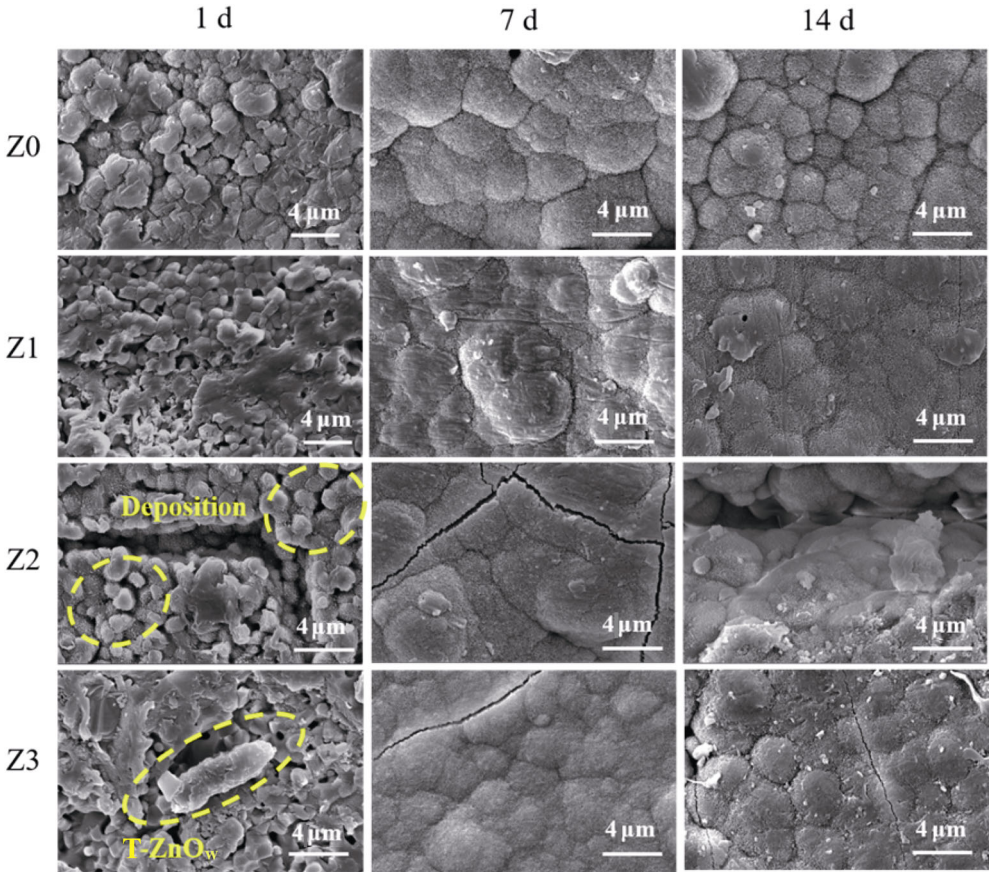

Fig. 11 SEM images of samples after soaking in SBF.

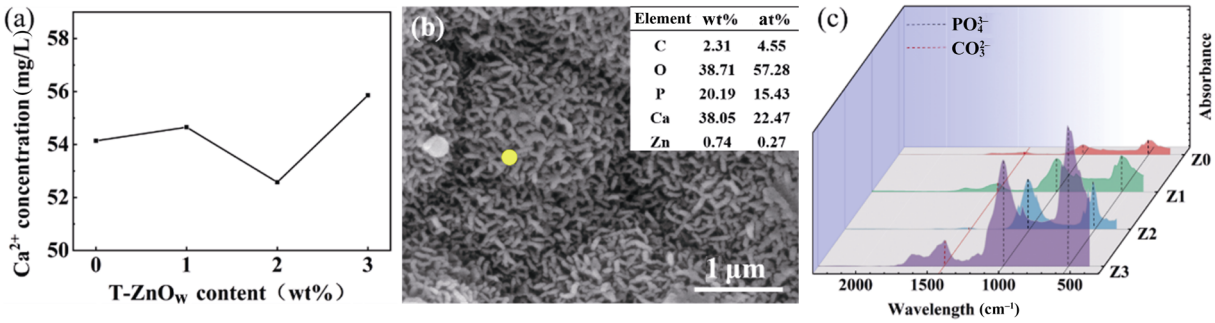

Fig. 12 (a) Ca^{2+} concentration in SBF after soaking samples for 1 d, (b) SEM image of sediment layer, and (c) FTIR analysis of the sample after soaking in SBF for 14 d.

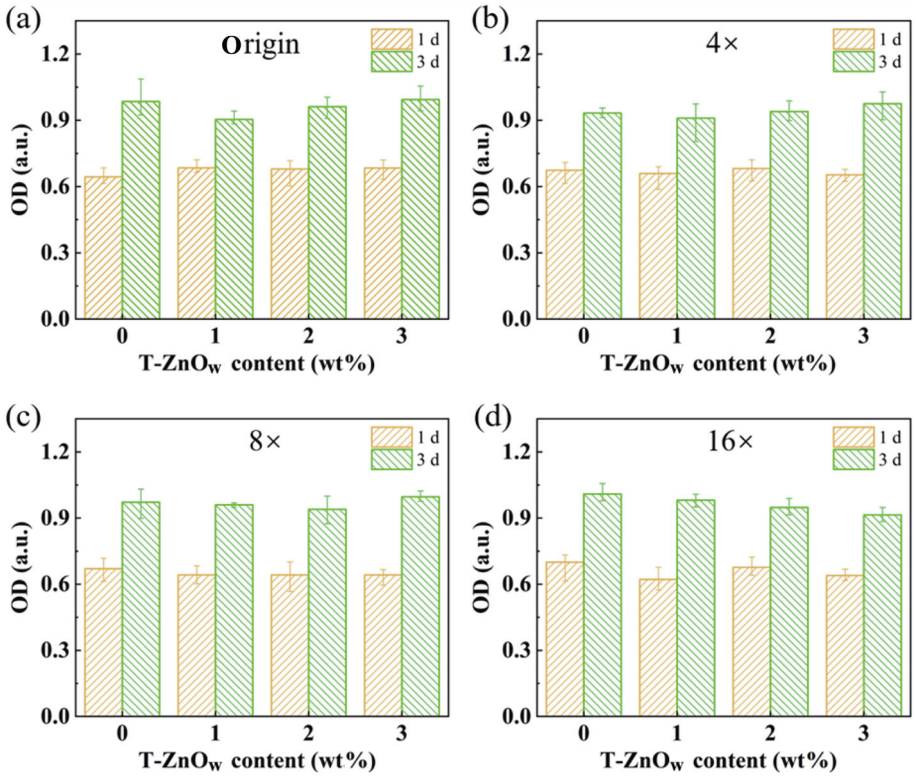

Fig. 13 CCK-8 results of MC-3T3 cultured with scaffold extraction fluid for 1 and 3 d: (a) origin extraction fluid, (b) 4-time dilution, (c) 8-time dilution, and (d) 16-time dilution.

various T-ZnO_w contents, indicating that current whisker contents are safe for cells.

4 Conclusions

In this work, T-ZnO_w enhanced BCP scaffolds with TPMS-based double-layer porous structure were successfully fabricated by DLP technology. With low viscosity and optimized exposure energy (12 mJ/cm^2), scaffolds were all printed with high precision.

After samples being sintered at 1200 ℃, the new phase $Ca_{19}Zn_2(PO_4)_{14}$ forms by the reaction between T-ZnO_w and β-TCP, and the phase transition to α-TCP is inhibited. With the increase of T-ZnO_w, the flexural strength first increases and then decreases. Z2 has the highest flexural strength (68.5 MPa) because T-ZnO_w could absorb energy and play the role of toughening. Excessive T-ZnO_w leads to low cure depth and poor combination between layers as well as more printing defects, which would cause the samples to break along layers during flexural test. In apatite forming test, Z2 shows the most Ca^{2+} deposition and the fastest mineralization rate after soaking for 1 d. After soaking

for 7 d, all samples mineralize completely. In *in vitro* test, the samples exhibit good biocompatibility since cells can proliferate well under different dilute times. These findings confirmed that BCP scaffolds doped by T-ZnO_w can be well-printed by DLP. The addition of T-ZnO_w can improve the mechanical property of composite scaffolds and keep good biological property, so that the composite scaffolds are hopeful to be used in personalized repair of bone defect.

Acknowledgements

This work was supported by the financial support from the Major Special Projects of Technological Innovation in Hubei Province (2019AAA002), the National Key R&D Program of China (2018YFB1105503), and Fundamental Research Funds for the Central Universities (2019kfyXMPY020, 2020kfyFPZX003, 2018KFYYXJJ030, and 2019kfyXKJC011). The authors would like to thank Chen-Min Yao and Xiao-Yi Wu from Hospital of Stomatology, Wuhan University for *in vitro* test, thank State Key Laboratory of Materials Processing and Die & Mould Technology for SEM and mechanical property tests, and also thank the Huazhong University of Science & Technology Analytical & Testing Center for XRD and FTIR tests.

Electronic Supplementary Material

Supplementary material is available in the online version of this article at https://doi.org/10.1007/s40145-021-0557-z.

References

[1] Campana V, Milano G, Pagano E, *et al*. Bone substitutes in orthopaedic surgery: From basic science to clinical practice. *J Mater Sci Mater Med* 2014, **25**: 2445–2461.

[2] Vorndran E, Moseke C, Gbureck U. 3D printing of ceramic implants. *MRS Bull* 2015, **40**: 127–136.

[3] Manzini BM, Machado LMR, Noritomi PY, *et al*. Advances in bone tissue engineering: A fundamental review. *J Biosci* 2021, **46**: 17.

[4] Ambekar RS, Kandasubramanian B. Progress in the advancement of porous biopolymer scaffold: Tissue engineering application. *Ind Eng Chem Res* 2019, **58**: 6163–6194.

[5] Hua SB, Su J, Deng ZL, *et al*. Microstructures and properties of 45S5 bioglass® & BCP bioceramic scaffolds fabricated by digital light processing. *Addit Manuf* 2021, **45**: 102074.

[6] Eliaz N, Metoki N. Calcium phosphate bioceramics: A review of their history, structure, properties, coating technologies and biomedical applications. *Materials* 2017, **10**: 334.

[7] Gao CD, Peng SP, Feng P, *et al*. Bone biomaterials and interactions with stem cells. *Bone Res* 2017, **5**: 17059.

[8] Dorozhkin SV. Biphasic, triphasic and multiphasic calcium orthophosphates. *Acta Biomater* 2012, **8**: 963–977.

[9] Shiota T, Shibata M, Yasuda K, *et al*. Influence of β-tricalcium phosphate dispersion on mechanical properties of hydroxyapatite ceramics. *J Ceram Soc Jpn* 2008, **116**: 1002–1005.

[10] Shuai CJ, Li PJ, Liu JL, *et al*. Optimization of TCP/HAP ratio for better properties of calcium phosphate scaffold via selective laser sintering. *Mater Charact* 2013, **77**: 23–31.

[11] Tampieri A, Iafisco M, Sandri M, *et al*. Magnetic bioinspired hybrid nanostructured collagen–hydroxyapatite scaffolds supporting cell proliferation and tuning regenerative process. *ACS Appl Mater Interfaces* 2014, **6**: 15697–15707.

[12] Meng J, Xiao B, Zhang Y, *et al*. Super-paramagnetic responsive nanofibrous scaffolds under static magnetic field enhance osteogenesis for bone repair *in vivo*. *Sci Rep* 2013, **3**: 2655.

[13] Kose N, Çaylak R, Pekşen C, *et al*. Silver ion doped ceramic nano-powder coated nails prevent infection in open fractures: *In vivo* study. *Injury* 2016, **47**: 320–324.

[14] Eto S, Miyamoto H, Shobuike T, *et al*. Silver oxide-containing hydroxyapatite coating supports osteoblast function and enhances implant anchorage strength in rat femur. *J Orthop Res* 2015, **33**: 1391–1397.

[15] Zhang JC, Huang D, Liu SF, *et al*. Zirconia toughened hydroxyapatite biocomposite formed by a DLP 3D printing process for potential bone tissue engineering. *Mater Sci Eng C* 2019, **105**: 110054.

[16] Wang WH, Yeung KWK. Bone grafts and biomaterials substitutes for bone defect repair: A review. *Bioact Mater* 2017, **2**: 224–247.

[17] Calhoun NR, Smith JC, Becker KL. The role of zinc in bone metabolism. *Clin Orthop Relat Res* 1974: 212–234.

[18] Zeng AR, Zheng YY, Guo Y, *et al*. Effect of tetra-needle-shaped zinc oxide whisker (T-ZnO_w) on mechanical properties and crystallization behavior of isotactic polypropylene. *Mater Des* 2012, **34**: 691–698.

[19] Yuan FY, Zhang HB, Li XF, *et al*. Synergistic effect of boron nitride flakes and tetrapod-shaped ZnO whiskers on the thermal conductivity of electrically insulating phenol formaldehyde composites. *Compos A Appl Sci Manuf* 2013, **53**: 137–144.

[20] Zhou ZW, Liu SK, Gu LX. Studies on the strength and wear resistance of tetrapod-shaped ZnO whisker-reinforced rubber composites. *J Appl Polym Sci* 2001, **80**: 1520–1525.

[21] Shuai CJ, Deng JJ, Gao CD, *et al*. Mechanisms of tetraneedlelike ZnO whiskers reinforced forsterite/bioglass

scaffolds. *J Alloys Compd* 2015, **636**: 341–347.
[22] Guo WH, Zhao FJ, Wang YD, *et al*. Characterization of the mechanical behaviors and bioactivity of tetrapod ZnO whiskers reinforced bioactive glass/gelatin composite scaffolds. *J Mech Behav Biomed Mater* 2017, **68**: 8–15.
[23] Kim D, Jang M, Seo J, *et al*. UV-cured poly(urethane acrylate) composite films containing surface-modified tetrapod ZnO whiskers. *Compos Sci Technol* 2013, **75**: 84–92.
[24] Choi SW, Zhang Y, Macewan MR, *et al*. Neovascularization in biodegradable inverse opal scaffolds with uniform and precisely controlled pore sizes. *Adv Healthc Mater* 2013, **2**: 145–154.
[25] Wu RH, Li YF, Shen MD, *et al*. Bone tissue regeneration: The role of finely tuned pore architecture of bioactive scaffolds before clinical translation. *Bioact Mater* 2021, **6**: 1242–1254.
[26] Barba D, Alabort E, Reed RC. Synthetic bone: Design by additive manufacturing. *Acta Biomater* 2019, **97**: 637–656.
[27] Ma SH, Song KL, Lan J, *et al*. Biological and mechanical property analysis for designed heterogeneous porous scaffolds based on the refined TPMS. *J Mech Behav Biomed Mater* 2020, **107**: 103727.
[28] Kaur I, Singh P. Flow and thermal transport characteristics of triply-periodic minimal surface (TPMS)-based gyroid and Schwarz-P cellular materials. *Numer Heat Transf A Appl* 2021, **79**: 553–569.
[29] Wu JM, Li M, Liu SS, *et al*. Selective laser sintering of porous Al_2O_3-based ceramics using both Al_2O_3 and SiO_2 poly-hollow microspheres as raw materials. *Ceram Int* 2021, **47**: 15313–15318.
[30] Liu SS, Li M, Wu JM, *et al*. Preparation of high-porosity Al_2O_3 ceramic foams via selective laser sintering of Al_2O_3 poly-hollow microspheres. *Ceram Int* 2020, **46**: 4240–4247.
[31] Ashwin AJ, Jafferson JM. State of the art direct ink writing (DIW) and experimental trial on DIW of HAp bio-ceramics. *Mater Today Proc* 2021, **46**: 1298–1307.
[32] Li H, Liu YS, Liu YS, *et al*. Effect of sintering temperature in argon atmosphere on microstructure and properties of 3D printed alumina ceramic cores. *J Adv Ceram* 2020, **9**: 220–231.
[33] Chen F, Zhu H, Wu JM, *et al*. Preparation and biological evaluation of ZrO_2 all-ceramic teeth by DLP technology. *Ceram Int* 2020, **46**: 11268–11274.
[34] Yao YX, Qin W, Xing BH, *et al*. High performance hydroxyapatite ceramics and a triply periodic minimum surface structure fabricated by digital light processing 3D printing. *J Adv Ceram* 2021, **10**: 39–48.
[35] Chen ZW, Li ZY, Li JJ, *et al*. 3D printing of ceramics: A review. *J Eur Ceram Soc* 2019, **39**: 661–687.
[36] Chen Z, Sun XH, Shang YP, *et al*. Dense ceramics with complex shape fabricated by 3D printing: A review. *J Adv Ceram* 2021, **10**: 195–218.
[37] Feng CW, Zhang KQ, He RJ, *et al*. Additive manufacturing of hydroxyapatite bioceramic scaffolds: Dispersion, digital light processing, sintering, mechanical properties, and biocompatibility. *J Adv Ceram* 2020, **9**: 360–373.
[38] Li YH, Wang ML, Wu HD, *et al*. Cure behavior of colorful ZrO_2 suspensions during digital light processing (DLP) based stereolithography process. *J Eur Ceram Soc* 2019, **39**: 4921–4927.
[39] Zheng JT, Zhang H, Li X. Effect of ternary particles size distribution on rheology of slurry and microstructure of DLP printed ZTA ceramic. *Mater Chem Phys* 2021, **269**: 124656.
[40] Li XB, Zhong H, Zhang JX, *et al*. Fabrication of zirconia all-ceramic crown via DLP-based stereolithography. *Int J Appl Ceram Technol* 2020, **17**: 844–853.
[41] Peng PF, Wang F, Liao QL, *et al*. Effect of T-ZnO_w addition on the degradability of sol–gel derived SiO_2–CaO–P_2O_5 glass-ceramics. *J Non Cryst Solids* 2020, **529**: 119798.
[42] Li Z, Yang RS, Yu M, *et al*. Cellular level biocompatibility and biosafety of ZnO nanowires. *J Phys Chem C* 2008, **112**: 20114–20117.
[43] Ghaffari M, Moztarzadeh F, Safavi M. A comparative study on the shape-dependent biological activity of nanostructured zinc oxide. *Ceram Int* 2019, **45**: 1179–1188.
[44] Bagheri Saed A, Behravesh AH, Hasannia S, *et al*. Functionalized poly L-lactic acid synthesis and optimization of process parameters for 3D printing of porous scaffolds via digital light processing (DLP) method. *J Manuf Process* 2020, **56**: 550–561.
[45] Bagheri Saed A, Behravesh AH, Hasannia S, *et al*. An *in vitro* study on the key features of poly L-lactic acid/biphasic calcium phosphate scaffolds fabricated via DLP 3D printing for bone grafting. *Eur Polym J* 2020, **141**: 110057.
[46] Tomeckova V, Halloran JW. Flow behavior of polymerizable ceramic suspensions as function of ceramic volume fraction and temperature. *J Eur Ceram Soc* 2011, **31**: 2535–2542.
[47] Borlaf M, Serra-Capdevila A, Colominas C, *et al*. Development of UV-curable ZrO_2 slurries for additive manufacturing (LCM-DLP) technology. *J Eur Ceram Soc* 2019, **39**: 3797–3803.
[48] Scialla S, Carella F, Dapporto M, *et al*. Mussel shell-derived macroporous 3D scaffold: Characterization and optimization study of a bioceramic from the circular economy. *Mar Drugs* 2020, **18**: 309.
[49] Fukuda A, Takemoto M, Saito T, *et al*. Osteoinduction of porous Ti implants with a channel structure fabricated by selective laser melting. *Acta Biomater* 2011, **7**: 2327–2336.
[50] Serena S, Carbajal L, Sainz MA, *et al*. Thermodynamic assessment of the system CaO–P_2O_5: Application of the ionic two-sublattice model to glass-forming melts. *J Am Ceram Soc* 2011, **94**: 3094–3103.
[51] Carbajal L, Serena S, Caballero A, *et al*. Role of ZnO additions on the β/α phase relation in TCP based materials: Phase stability, properties, dissolution and biological

response. *J Eur Ceram Soc* 2014, **34**: 1375–1385.
[52] Romeis S, Hoppe A, Eisermann C, *et al*. Enhancing *in vitro* bioactivity of melt-derived 45S5 bioglass® by comminution in a stirred media mill. *J Am Ceram Soc* 2014, **97**: 150–156.
[53] Syazwan MNM, Ahmad-Fauzi MN, Balestri W, *et al*. Effectiveness of various sintering aids on the densification and *in vitro* properties of carbonated hydroxyapatite porous scaffolds produced by foam replication technique. *Mater Today Commun* 2021, **27**: 102395.